Geophys. J. Int. (2004) **158,** 899–912 doi: 10.1111/j.1365-246X.2004.02347.x

Source discriminants for near-field tsunamis

Emile A. Okal[1] and Costas E. Synolakis[2]

[1] *Department of Geological Sciences, Northwestern University, Evanston,* IL 60201, *USA*
[2] *Department of Civil Engineering, University of Southern California, Los Angeles,* CA 90089, *USA*

Accepted 2004 March 31. Received 2004 March 29; in original form 2003 November 12

SUMMARY

We present numerical simulations of tsunami run-up in the near field for a data set of 72 models of sources, involving both seismic dislocations and landslides. By varying one by one the parameters describing the source and the receiving beach, we are able to separate their individual influence on the amplitude and distribution of run-up, which we characterize by forming several dimensionless parameters, principally the ratio I_2 of its maximum amplitude to its lateral extent along the beach. We find that I_2 remains less than 10^{-4} for seismic dislocation sources but is greater than this threshold for all physically realistic models of underwater landslides. Thus, it can be used as a discriminant for the nature of the source of a near-field tsunami. For seismic dislocations, we also consider the ratio I_1 of maximum run-up to seismic slip on the fault plane, and validate numerically the previously suggested 'rule of thumb' that this ratio cannot be much greater than 1. In the case of underwater landslides, we show that the distribution of near-field run-up is primarily controlled by the 2-D 'wall of water' displaced on the ocean surface as an initial condition to the simulation, and is practically independent of its extension in the third dimension, perpendicular to the beach.

We apply this approach to nine profiles of tsunami run-up obtained experimentally during recent field surveys, and show that our method successfully identifies the 1998 Papua New Guinea tsunami as having been generated by an underwater landslide, thus confirming the results of shipboard and hydroacoustic investigations. It also strongly suggests a similar mechanism for the generation of the near-field Aleutian tsunami of 1946 April 1.

Key words: near-field, simulations, tsunamis, tsunami surveys.

1 INTRODUCTION AND BACKGROUND

The purpose of this paper is to define robust discriminants allowing the identification of the physical nature of the source of a tsunami, based on the distribution of run-up amplitudes along a coastline in the near field. We are motivated by two relatively recent developments: first, the recognition of the importance of underwater landslides as prominent generators of locally devastating tsunamis, and second, the recent availability of detailed data sets of run-up amplitudes along coastlines following field surveys which have become systematic in the aftermath of major tsunamis (Okal *et al.* 2003a).

While the contribution of underwater landslides to the generation of tsunamis was known to such visionaries as Milne (1898) and Montessus de Ballore (1907), and was forcefully argued by Gutenberg (1939), it was not until the disastrous Aitape, Papua New Guinea (PNG) tsunami of 1998 July 17 that interest in landslide-triggered tsunamis was revived amongst scientists. The PNG tsunami, which involved waves of up to 15 m and resulted in 2200 deaths, could not be satisfactorily modelled as directly generated by the associated earthquake on several accounts:

(1) The disparity between the amplitude of run-up (consistently 10 m on the Sandaun coast of PNG) and the probable slip on the earthquake fault, as inferred under generally accepted scaling laws (Geller 1976) from the relatively moderate size of the parent earthquake ($M_0 = 3.7 \times 10^{26}$ dyn cm).

(2) The concentration of large run-up, and hence of death and destruction, along a short segment (23 km) of the Sandaun coast.

(3) The strong disparity between the disastrous character of the tsunami in the near field, and its benign nature in the far field, where it was recorded at amplitudes not exceeding 20 cm in Japan, and remained undetected in Hawaii.

(4) The timing of the wave itself, which was reported by survivors as arriving at least 10 min too late to have been generated by the seismic main shock.

Rather, and based in particular on the analysis of hydroacoustic signals recorded off Wake Island (Okal 2003a), Synolakis *et al.* (2002a) proposed that the 1998 Aitape tsunami was generated by a major underwater landslide, occurring 13 min after the seismic main shock, at a location where shipboard surveys indeed recognized a fresh slump with a volume of 4 km^3 (Sweet & Silver 2003).

Both the documented occurrence of damaging landslide-triggered tsunamis (e.g. at Skagway in 1994, Kulikov *et al.* 1996; Synolakis *et al.* 2002b), and the recognition of massive landslide scars in the underwater neighbourhood of heavily populated areas (Lee *et al.*

2003) have led to a renewed effort in assessing the regional tsunami hazard from underwater landslides (e.g. Borrero *et al.* 2001). In this context, it is important to understand the contribution, if any, of potential landslides as generators of major recent tsunamis, based on the extensive data sets gathered during post-tsunami surveys.

We are guided in the present study by a few simple concepts. While the amplitude ζ of run-up at a single location along a real-life beach will be affected by local factors such as bays, estuaries or land use (development, vegetation, etc.), we note that, along an idealized linear shoreline featuring translational symmetry in the y direction, the maximum amplitude of run-up, $b = \max_y \zeta(y)$, should be related to the initial amplitude of deformation of the sea surface in the generation area, and hence to the vertical deformation z of the ocean floor at the source. In addition, the lateral extent of sustained run-up along the beach, a, should express the lateral dimension D of the area of underwater deformation of the ocean floor at the source.

In the case of an earthquake dislocation, and regardless of the influence of source parameters such as focal geometry and depth, scaling laws essentially express the invariance of stress drop, or assuming constant rigidity, of strain release. Rocks fail seismically because their deformation under tectonic forces overcomes their strength, at a critical strain $\varepsilon_{\max}$, typically of the order of 10^{-4}. While this value can fluctuate slightly, its order of magnitude is limited by the nature of crustal rocks. In practice, large earthquakes ($M_0 \approx 10^{28}$ dyn cm) feature slips Δu of one to a few metres and fault dimensions of $\sim$100 km, with exceptional shocks (e.g. Chile 1960, Alaska 1964) reaching 20 m of slip over 800 km of fault length (Plafker 1965; Plafker & Savage 1970). This limit $\varepsilon_{\max}$ would be expected to translate into a limit on the aspect ratio b/a of the run-up distribution $\zeta(y)$.

The situation is quite different for underwater landslides, which involve a breakdown in the cohesion of the material. As a result, the vertical deformation of the ocean floor z can reach several hundred metres over dimensions D not exceeding a few to a few tens of kilometres. Thus, and based on general scaling arguments ignoring structural details on the receiving shore, we anticipate that the distribution of run-up along a beach, in other words the aspect ratio of the curve $\zeta(y)$, may differ fundamentally, possibly by several orders of magnitude, when considering tsunamis generated by landslides as opposed to dislocations.

The goal of this paper is to justify and quantify this intuitive concept through systematic numerical simulations of run-up on a nearby shore, for an extensive number of dislocation and landslide sources. We define the aspect ratio $I_2 = b/a$ as a discriminant for the nature of the source and we verify its performance on a data set of nine run-up profiles gathered during recent surveys in the aftermath of major tsunamis.

2 MODELS

The general geometry of our simulations is shown in Fig. 1. We consider a linear beach oriented along y, sloping at an angle β into an oceanic basin of uniform depth H. To facilitate the description, the direction of positive y on Fig. 1 will be referred to as 'east'. Our purpose is to study the amplitude and distribution of run-up $\zeta(y)$ on the beach, as a function of the coordinate y for a variety of source and model geometries.

2.1 Dislocations

In the case of dislocations, we position an earthquake source at distance L from the beach, and depth h below the ocean bottom.

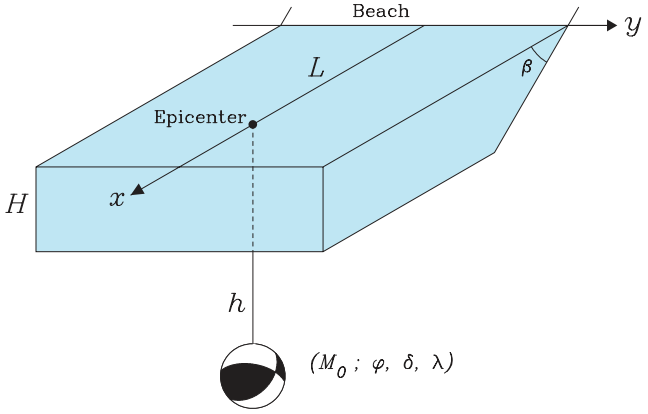

Figure 1. Sketch of the geometry of our simulation experiments, illustrated for the case of a dislocation source. The structure (ocean, beach, substratum) has translational symmetry along y. The ocean is shown as the shaded body of water. See text for details.

The source is a double-couple of moment M_0, fault strike ϕ, dip angle δ and slip angle λ, the conventions being those of the Harvard Catalog (Dziewonski *et al.* 1983). Thus, there are *a priori* eight variable parameters in the problem: the model parameters H and β, the source location parameters L and h, the source orientation angles ϕ, δ and λ and the source size M_0.

In real life, and for each new earthquake source, many if not all such parameters are expected to vary. Thus, individual simulations run on a small number of natural sources have been unable to gain insight into the influence of each individual source parameter. In addition, most theoretical studies of the factors controlling tsunami excitation, such as that of Pod"yapol'skii (1970) or Yamashita & Sato (1974), let only a limited number of parameters vary, ignoring, for example, variations in beach slope or distance from the source to the receiving coastline. (Note also that the latter study is cast in a far-field formalism.)

In the present investigation we shall let each source parameter in our simulation vary separately in order to isolate and study its individual influence on the amplitude and distribution of run-up along the coast. It could be tempting to regroup these parameters into those characterizing the source (e.g. the total volume of water displaced) and those describing its location with respect to the beach model. However, the exact nature of such combinations may be unclear, as Satake & Kanamori (1991), and more recently Satake & Tanioka (2003), have argued that the potential energy of the initial ground displacement can be a better estimator of run-up in the near field (or for landslide sources) than the total volume of water displaced (usable for dislocation sources or in the far field). In addition, the influence of the proposed two groups on the observable run-up along the coast is not necessarily separable, and thus we prefer to study each parameter individually.

For each set of dislocation source parameters, we interpret the scalar moment M_0 in terms of seismic slip Δu and fault dimensions, using the scaling laws of Geller (1976). After positioning the finite source below the ocean floor as a function of the parameters L and h, we compute the field of vertical static deformation over a 600 $\times$ 600 km section of the ocean floor, using the algorithm of Mansinha & Smylie (1971). The example shown in Fig. 2(a) involves a large shallow dipping thrust fault ($\phi = 270^\circ$, $\delta = 30^\circ$, $\lambda = 90^\circ$), characteristic of interplate subduction events. Its moment is $M_0 = 2 \times 10^{28}$ dyn cm, corresponding to a slip $\Delta u = 4.1$ m, and to a fault rupture area of 140 by 70 km. The initiation of rupture

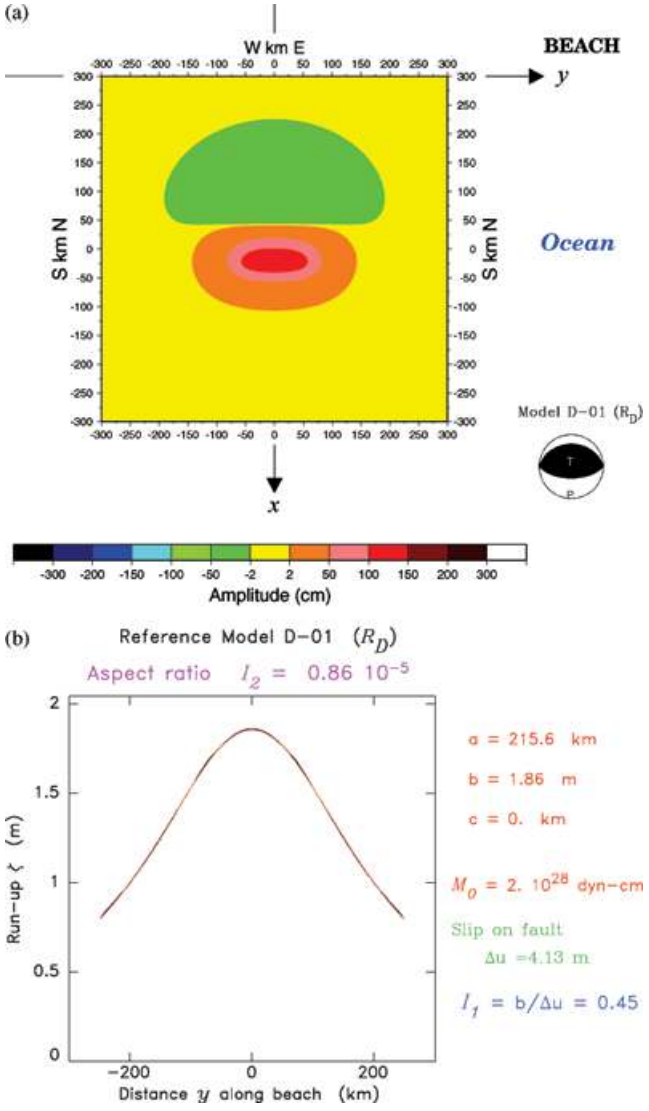

Figure 2. (a) Reference model (D-01) for dislocation sources. The main panel shows the static deformation of the ocean floor, used as the initial condition of the hydrodynamic simulation. Axes x and y are the same as in Fig. 1. The 'beach ball' on the right sketches the geometry of the focal mechanism used. (b) Result of hydrodynamic simulation for reference model D-01. The black line shows the individual values of run-up ζ computed along the beach. The red line is the best-fitting curve of the form of eq. (1), with parameters a, b and c listed on the right. The scalars I_1 and I_2 are also given.

occurs at $h = 35$ km, and the centroid of rupture is located at $L = 300$ km. This particular geometry (Model D-01) will be taken as a reference dislocation (R_D in Table 1) against which all other cases will be assessed.

In practice, the deformation of the ocean floor takes place faster than the tsunami can propagate the resulting surface disturbance (the two velocities to be compared in this respect are the velocity of propagation of rupture along the fault, V_R, and the group velocity C of the tsunami; in all circumstances, and even for the so-called 'tsunami earthquakes' (Kanamori & Kikuchi 1993), one has $V_R \gg C$). It is then legitimate to directly translate the ocean-bottom deformation to the water surface, and to use it as an initial condition in our hydrodynamic simulations. The latter are carried out using the MOST code (Titov & Synolakis 1998), which solves the non-linear shallow water wave equations on a variable staggered grid with the method of fractional steps; the code calculates the maximum penetration of the wave onto the sloping beach represented in Fig. 1. Run-up ζ is defined at each point y along the beach as the vertical elevation above the undeformed water level over initially dry land. The computation is performed using a final grid as fine as 150 m, but the results are kept only at steps $\delta y = 1.5$ km. Fig. 2(b) shows (in black) the distribution $\zeta(y)$ along the shoreline.

We elect to characterize its shape by empirically fitting a formula of the type

$$\zeta(y) = \frac{b}{[(y-c)/a]^2 + 1}, \tag{1}$$

where the parameters a, b and c are optimized by trial and error. The red curve on Fig. 2(b) is the best-fitting distribution (eq. 1); note that in this case, the fit is essentially perfect.

We then consider the two dimensionless quantities

$$I_1 = \frac{b}{\Delta u} \quad \text{and} \quad I_2 = \frac{b}{a}. \tag{2}$$

I_1 scales the maximum run-up on the beach to the amplitude of seismic slip on the fault; I_2 characterizes the aspect ratio of the distribution of run-up on the beach. We anticipate that these scalars may be largely invariant upon changes in the model parameters.

2.2 Landslides

In the case of landslides, we are inspired by the deformation field used by Synolakis *et al.* (2002a) to model the PNG landslide, based on shipboard surveys by Sweet & Silver (2003). As shown in Fig. 3, the source is dipolar in nature, the surface of the ocean featuring a negative depression (trough), and a positive elevation (hump) farther from the shore. While the use of a dipolar source constitutes only an approximation to the full description of the dynamic evolution of a sliding mass on the bottom of the ocean, we note the general agreement obtained in the case of PNG between models using a dipolar representation of the source (Synolakis *et al.* 2002a) and detailed dynamic models of the sliding mass (Heinrich *et al.* 2000).

Furthermore, analytical solutions obtained in the simple case of the translation of a mass on a flat ocean bottom also show the development of essentially dipolar waves at the ocean surface (Tinti & Bortolucci 2000; Okal & Synolakis 2003). However, and because of the relatively slow propagation of an underwater landslide on the ocean floor, at velocities observed to be much slower than the wave's group velocity, i.e. at generally low Froude numbers (Schwarz 1982), the amplitude η_- of the depression (taken as negative) is in absolute value considerably less than the actual deformation z of the ocean floor. The shape of the trough is modelled using a hyperbolic cross-section of the form $\mathrm{sech}(\alpha_- y) \times \mathrm{sech}(\gamma_- x)$. The elevation, displaced a distance l (the lever of the dipole) from the trough, can feature a smaller amplitude η_+ and lesser values of the coefficients α_+ and γ_+. This asymmetric character of the dipole reflects the scattering of the sliding material, which loses its cohesion at least partially during the landslide. Note that the total volumes of the initial depression and elevation,

$$\left(\frac{\pi^2}{4}\frac{\eta_-}{\alpha_-\gamma_-}\right) \quad \text{and} \quad \left(\frac{\pi^2}{4}\frac{\eta_+}{\alpha_+\gamma_+}\right)$$

should balance. All the above parameters describing the shape of the source ($\eta_\pm$, $\alpha_\pm$, $\gamma_\pm$, l), its location and orientation with respect to the beach (L and the azimuth ϕ of its lever), as well as the structural parameters H and β (Fig. 1), can be varied.

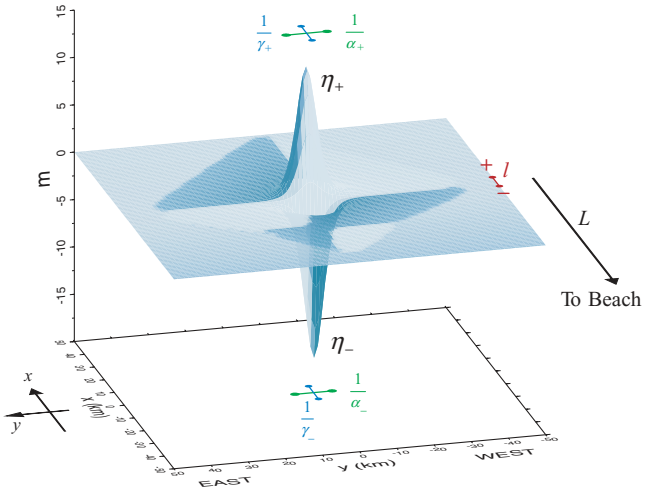

Figure 3. 3-D sketch of initial surface deformation for reference landslide model L-01. The model consists of a depression of (negative) amplitude η_- combined with an elevation of amplitude η_+, displaced away from the beach along a lever l. The cross-sections of the initial depression (resp. elevation) are sech functions, of characteristic widths $1/\alpha_-$ (in the y direction) and $1/\gamma_-$ (in the x direction) (resp. $1/\alpha_+$ and $1/\gamma_+$). The centre of the dipole is positioned at a distance L from the beach.

The modelling then proceeds as in the case of a dislocation, and Fig. 4 is conceptually similar to Fig. 2. Note, however, that the calculation is carried out on a finer grid and involves a shorter segment of beach. The same function is used to fit the distribution $\zeta(y)$, and we study the invariance of the dimensionless scalars

$$I_2 = \frac{b}{a} \quad \text{and} \quad I_3 = -\frac{b}{\eta_-}. \tag{3}$$

I_2 has the same definition as for a dislocation source, and I_3 scales the maximum run-up on the beach to the amplitude of the initial depression on the ocean surface.

3 RESULTS OF SIMULATIONS

3.1 Dislocations

Results are given in Table 1, in the form of the two scalars I_1 and I_2. At the top of the table, the reference model (R_D) described on Fig. 2 is summarized. Then for each parameter varied, this model is repeated (R_D) and a number of other values are examined.

3.1.1 Size (moment M_0) of the earthquake

Both scalars are found to increase with M_0. This can be understood by noting that, for a constant distance L from the shore to the centroid of rupture, an increase in earthquake size enlarges the rupture area, which extends closer to the beach and hence reduces the scatter in the wave amplitude due to propagation, leading to an increase in I_1. Similarly, because the deformation field at the source is closer to the shore, the distribution of run-up is less scattered along the beach, resulting in an enhanced value of I_2.

3.1.2 Source depth, h

This constitutes a rather sensitive issue since intuition in earlier studies generally assumed that tsunami generation was critically

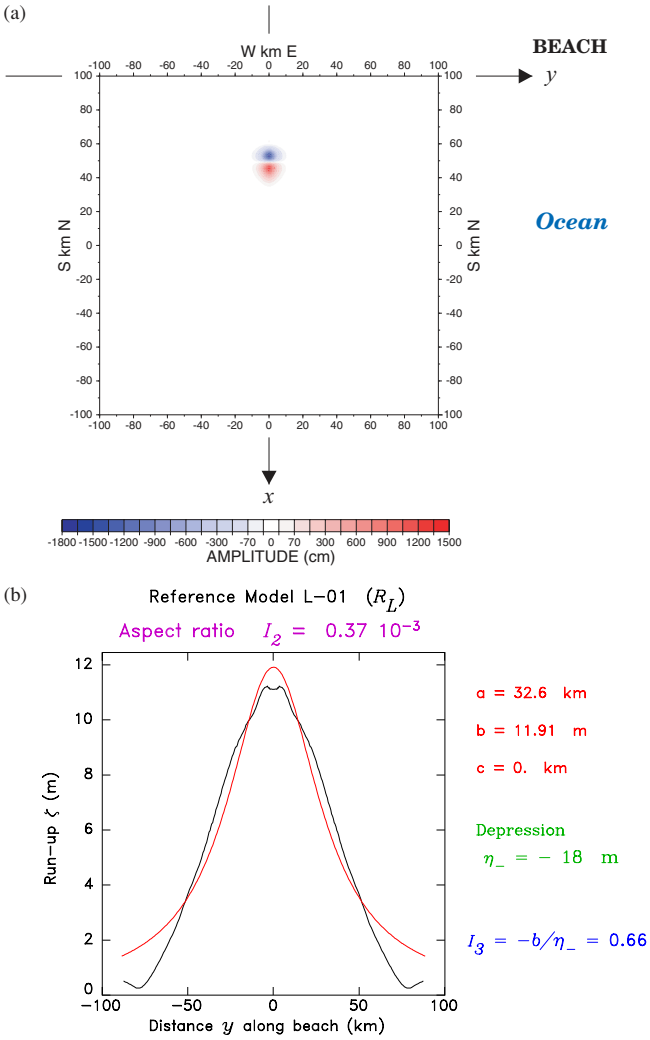

Figure 4. (a) Initial field of deformation of the ocean surface for the hydrodynamic simulation of Model L-01. Note the different scale of this map view, as compared with Fig. 2(a). (b) Same as Fig. 2(b) for the landslide reference model L-01. While the plotting conventions are the same, the scale of both the y and ζ axes is different, resulting in a much greater value of the aspect ratio I_2.

enhanced by shallow source depths (e.g. Ewing *et al.* 1950). However, on the basis of normal mode theory, Ward (1980, 2002) and Okal (1988) have argued that the amplitudes of far-field tsunamis depend only weakly on earthquake depth, reflecting the large wavelengths and skin depths of the eigenfunctions of the relevant modes. Their formalism does not apply in the near field, though, where this question must be investigated separately. Table 1 shows that both scalars I_1 and I_2 vary only moderately (by a factor of 1.6) when h varies from 5 to 45 km. The explanation of this result is that, for large earthquakes bearing tsunamigenic risk and obeying scaling laws, the width W of the source is at least several tens of kilometres, which in a sense precludes the existence of a large, entirely shallow, earthquake. This interpretation is verified in Models D-10 and D-11 by considering the same variation in depth (5 and 45 km, respectively), but for an event featuring the smaller moment of Model D-02 ($M_0 = 2 \times 10^{27}$ dyn cm). As seen in Table 1, I_1 and I_2 now vary more substantially between 5 and 45 km (by factors of 2.93 and 3.45 respectively). Note that this result assumes the simple model of a

Table 1. Model characteristics and invariants I_1 and I_2 for dislocation sources.

Parameter varied	Model	b (m)	I_1	I_2
	D-01 (reference) (R_D)	1.86	0.45	0.86×10^{-5}
1. Size: seismic moment, M_0 (dyn cm)				
$M_0 = 2 \times 10^{27}$	D-02	0.42	0.22	0.18×10^{-5}
$M_0 = 5 \times 10^{27}$	D-03	0.82	0.32	0.37×10^{-5}
$M_0 = 1 \times 10^{28}$	D-04	1.28	0.39	0.60×10^{-5}
$M_0 = 2 \times 10^{28}$	D-01 (R_D)	1.86	0.45	0.86×10^{-5}
$M_0 = 5 \times 10^{28}$	D-05	2.99	0.53	1.30×10^{-5}
2. Depth: source depth, h (km)				
$h = 5$	D-06	2.54	0.62	1.2×10^{-5}
$h = 15$	D-07	2.41	0.58	1.04×10^{-5}
$h = 25$	D-08	2.21	0.54	1.01×10^{-5}
$h = 35$	D-01 (R_D)	1.86	0.45	0.86×10^{-5}
$h = 45$	D-09	1.59	0.38	0.74×10^{-5}
$h = 5$	D-10 ($M_0 = 2 \times 10^{27}$ dyn cm)	0.78	0.41	0.38×10^{-5}
$h = 45$	D-11 ($M_0 = 2 \times 10^{27}$ dyn cm)	0.27	0.14	0.11×10^{-5}
3. Dip: fault dip, δ				
$\delta = 10^\circ$	D-12	2.32	0.56	1.20×10^{-5}
$\delta = 20^\circ$	D-13	2.12	0.51	1.04×10^{-5}
$\delta = 30^\circ$	D-01 (R_D)	1.86	0.45	0.86×10^{-5}
$\delta = 45^\circ$	D-14	1.58	0.38	0.70×10^{-5}
$\delta = 60^\circ$	D-15	1.25	0.30	0.54×10^{-5}
$\delta = 90^\circ$	D-16	0.69	0.17	0.33×10^{-5}
4. Slip: fault slip, λ				
$\lambda = 30^\circ$	D-17	1.26	0.31	0.70×10^{-5}
$\lambda = 45^\circ$	D-18	1.51	0.37	0.77×10^{-5}
$\lambda = 60^\circ$	D-19	1.72	0.42	0.83×10^{-5}
$\lambda = 90^\circ$	D-01 (R_D)	1.86	0.45	0.86×10^{-5}
5. Strike: fault strike, ϕ				
$\phi = 270^\circ$	D-01 (R_D)	1.86	0.45	0.86×10^{-5}
$\phi = 285^\circ$	D-20	1.87	0.45	0.86×10^{-5}
$\phi = 300^\circ$	D-21	1.78	0.43	0.80×10^{-5}
6. Distance: distance to shore, L (km)				
$L = 100$	D-22	2.86	0.69	2.90×10^{-5}
$L = 200$	D-23	2.34	0.57	1.59×10^{-5}
$L = 300$	D-01 (R_D)	1.86	0.45	0.86×10^{-5}
$L = 400$	D-24	1.63	0.39	0.57×10^{-5}
7. Water depth: depth to ocean floor, H (m)				
$H = 5000$	D-01 (R_D)	1.86	0.45	0.86×10^{-5}
$H = 4000$	D-25	1.69	0.41	0.76×10^{-5}
$H = 3000$	D-26	1.46	0.35	0.65×10^{-5}
$H = 2000$	D-27	1.19	0.29	0.52×10^{-5}
8. Beach slope: beach slope to 5000 m, tan β				
tan $\beta = 1/50$	D-28	2.87	0.69	1.54×10^{-5}
tan $\beta = 1/30$	D-29	2.28	0.55	1.12×10^{-5}
tan $\beta = 1/20$	D-01 (R_D)	1.86	0.45	0.86×10^{-5}
tan $\beta = 1/13$	D-30	1.51	0.36	0.68×10^{-5}
9. Composite beaches: tan β_{up}; tan β_{down}				
1/20; 1/20	D-01 (R_D)	1.86	0.45	0.86×10^{-5}
1/50; 1/20 to 800 m	D-31	2.67	0.65	1.30×10^{-5}
1/13; 1/30 to 800 m	D-32	1.57	0.38	0.74×10^{-5}
1/100; 1/30 to 250 m	D-33	3.01	0.73	1.42×10^{-5}
10. 'Worst case' scenario	D-34	7.55	1.35	6.74×10^{-5}

homogeneous elastic substratum; the presence of a weak 'sedimentary' layer of lower rigidity would increase the static displacements and hence the tsunami heights in the near field, just as Okal (1988) has shown that it can significantly increase the excitation of far-field tsunamis.

3.1.3 Fault dip, δ

We find that a reduction in dip angle can result in a modest increase in I_1 and I_2, primarily because a lower value of δ results in a shallower average depth of the rupture area, and thus a larger static

displacement above the source. Note that a pure dip-slip on a vertical fault ($\delta = 90^\circ$) is a particularly inefficient tsunami generator ($I_1 = 0.17$). This result is expected in the context of normal mode theory (Ward 1980; Okal 1988), where it expresses the asymptotic singularity in excitation of the transverse moment tensor components M_{zx} and M_{zy} as $h \to 0$, for all modes at all frequencies; in the limit $h = 0$, the resulting seismogram (including any tsunami mode) would be identically zero at all times and all distances.

3.1.4 Fault slip, λ

We let λ vary to investigate the case of oblique convergence at subduction zones, as illustrated for example during the recent PNG earthquakes (Synolakis *et al.* 2002a; Borrero *et al.* 2003) or in the case of the large 1965 Rat Island earthquake (Wu & Kanamori 1973). Not surprisingly, we find that a component of strike-slip, which reduces vertical static displacement, lowers the value of I_1 while leaving I_2 practically unaffected. Pure strike-slip solutions ($\lambda = 0$), which classically feature a weak quadrupolar static field, lead to a run-up distribution with low amplitudes which cannot be satisfactorily fitted using eq. (1).

3.1.5 Fault strike, ϕ

In this group of experiments, we keep the azimuth of strike ϕ within 30° of the coastline, to account for the generally limited departure observed between those two directions. Fault strike is found to have only a minimal impact on the scalars I_1 and I_2.

3.1.6 Distance, L

This parameter is found to have a significant effect on I_1, and especially on I_2, which decreases by a factor of 5 when L increases from 100 to 400 km. This merely expresses the more pronounced evolution of the wave front away from the source for greater values of L.

3.1.7 Ocean depth, H

Next, we vary the depth of the ocean basin, while keeping all other parameters constant, including the slope of the beach. We find that the deeper basin results in larger and more focused run-ups (increased values of I_1 and I_2). Note that the former result is in general agreement with the result of Okal (2003b) in the far field, namely that the energy carried by the full tsunami wave is practically independent of H. Then, and everything else being equal, a deeper ocean basin results in a stronger shoaling effect between the high seas and the shoreline (see e.g. Green's law, Green 1838; Synolakis 1991). The effect on I_2 is entirely attributable to the increase in b (from 1.20 to 1.86 m between $H = 2000$ and 5000 m), while a remains essentially constant (varying only from 230 to 216 km).

3.1.8 Beach slope, β

We pursue this investigation in the next group of experiments, by varying the slope of the beach. We find that a gentler slope increases both scalars I_1 and I_2, by providing a longer, more progressive channel for shoaling which presumably reduces the amount of energy reflected back into the ocean. As in the case of variable basin depth H, the change in I_2 is mostly controlled by that in b (and hence I_1).

3.1.9 The case of composite beaches

We then investigate the case of a composite beach, where the slope breaks and becomes more gentle at a depth of 800 m. Such models are particularly relevant to the case of coastlines with extended continental shelves such as documented in Santa Monica Bay (Borrero *et al.* 2001) or in the Davidson Bank, between Unimak Island and the epicentre of the great 1946 Aleutian 'tsunami earthquake' (Okal *et al.* 2003b). In general, the addition of a more gently sloping section of beach nearest to the coast increases both scalars I_1 and I_2; this behaviour is consistent with the results of Kánoğlu *et al.* (1998).

These results strongly document that the relationship between the amplitude of a near-field tsunami on the high seas, in a flat basin of depth H, and the eventual run-up at the beach is controlled principally by the morphology of the slope, even in the simple 2-D model considered here. We show that the maximum b of the distribution of run-up $\zeta(y)$ on the beach is not only a function of the initial deformation of the ocean surface, but also of the shape of the beach on which the wave shoals. Thus it appears impossible to define a simple 'run-up amplification factor', allowing a universal transition between wave amplitude at depth H and eventual run-up at the shoreline. As such, formulae such as Green's law (Synolakis 1991), expressing the evolution of the amplitude of a propagating wave due to variation in bathymetry, may not be applicable during the ultimate interaction of the wave with the shoreline, where its amplitude can no longer be considered small as compared to the depth H (Synolakis & Skjelbreia 1993). Indeed, beyond the initial shoreline, the water depth coincides with the wave amplitude.

Finally, we define a 'worst case scenario', built specifically to achieve a large value of I_2. For this purpose, we consider a large earthquake ($M_0 = 5 \times 10^{28}$ dyn cm), featuring a relatively shallow dip ($\delta = 20^\circ$), placed $L = 150$ km from the shore in a basin of depth $H = 5000$ m, featuring a composite beach with slopes of 1/50 and 1/20 (as in Model D-31). We do not force even smaller values of epicentral depth or dip angle to remain within the range of geologically realistic parameters for truly great earthquakes. This model, D-34, leads to the largest values found for both I_1 (1.35) and I_2 (6.74×10^{-5}); note that the latter remains smaller than 10^{-4}.

The first conclusion of this test of 34 dislocation models is that the maximum run-up observed on a smooth beach (in the absence of pronounced bays, river estuaries and other topographic features enhancing run-up) remains *of the order of the slip on the fault*, Δu, even in the worst case scenario. This rule of thumb, proposed empirically by Plafker (1997), is confirmed numerically. The second conclusion is that under no condition does the scalar I_2 exceed the value of 10^{-4} generally associated with the maximum strain released during regular earthquakes, thus confirming the intuitive argument given in the Introduction.

3.2 Landslides

Results from landslide sources are presented in Table 2. The reference model (R_L) is computed for a basin depth of 5000 m, a beach slope with $\tan\beta = 1/20$, a depression $\eta_- = -18$ m and an elevation $\eta_+ = 15$ m, separated by a lever $l = 7$ km, with $\alpha_- = \alpha_+ = 0.3\ \mathrm{km}^{-1}$, $\gamma_- = 0.3\ \mathrm{km}^{-1}$ and $\gamma_+ = 0.25\ \mathrm{km}^{-1}$. The source is placed $L = 50$ km from the shore. Fig. 4 summarizes the initial displacement field and the result of our simulation, with the best available fit again shown in red. It is immediately clear that the aspect ratio scalar I_2 is about 30 times greater than for the reference dislocation model. We emphasize that the scales in Figs 4(a) and (b) are different from those in Figs 2(a) and (b).

Table 2. Model characteristics and invariants I_2 and I_3 for dislocation sources.

Parameter varied	Model	b (m)	I_2	I_3
	L-01 (reference) (R_L)	11.9	0.37×10^{-3}	0.66
1. Distance: distance from beach, L (km)				
$L = 25$	L-02	22.8	1.29×10^{-3}	1.27
$L = 50$	L-01 (R_L)	11.9	0.37×10^{-3}	0.66
$L = 75$	L-03	7.2	0.14×10^{-3}	0.40
$L = 100$	L-04	4.9	0.62×10^{-4}	0.27
2. Size of poles: depression η_-; elevation η_+ (m)				
−9; 7.5	L-05	5.7	0.17×10^{-3}	0.64
−18; 15	L-01 (R_L)	11.9	0.37×10^{-3}	0.66
−26; 21.7	L-06	17.2	0.44×10^{-3}	0.66
3. Dipole lever: lever, l (km)				
$l = 4$	L-07	7.4	0.23×10^{-3}	0.41
$l = 7$	L-01 (R_L)	11.9	0.37×10^{-3}	0.66
$l = 12$	L-08	15.8	0.44×10^{-3}	0.88
4. Dipole azimuth: lever strike, ϕ (°)				
$\phi = 180°$	L-01 (R_L)	11.9	0.37×10^{-3}	0.66
$\phi = 165°$	L-09	11.6	0.34×10^{-3}	0.64
$\phi = 150°$	L-10	10.8	0.27×10^{-3}	0.60
5. Source profile: α_-, α_+ , γ_- , γ_+ (km^{-1}); η_-, η_+ (m)				
0.3, 0.3, 0.3, 0.25; −18, 15	L-01 (R_L)	11.9	0.37×10^{-3}	0.66
0.15, 0.15, 0.3, 0.25; −9, 7.5	L-11 [spread along y, scaled 1/2]	11.3	0.45×10^{-3}	1.25
0.15, 0.15, 0.15, 0.125; −9, 7.5	L-12 [spread along x and y; scaled 1/2]	11.9	0.37×10^{-3}	1.32
0.15, 0.15, 0.15, 0.125; −4.5, 3.75	L-13 [spread along x and y; scaled 1/4]	5.7	0.17×10^{-3}	1.27
0.6, 0.6, 0.6, 0.5; −18, 15	L-14 [peaked; unscaled]	3.8	0.12×10^{-3}	0.21
0.6, 0.6, 0.6, 0.5; −72, 60	L-15 [peaked; scaled 4]	15.3	0.49×10^{-3}	0.21
0.6, 0.6, 0.6, 0.5; −36, 30	L-16 [peaked along y; scaled 2]	12.1	0.34×10^{-3}	0.34
0.15, 0.15, 0.15, 0.125; −18, 15	L-17 [spread; unscaled]	23.2	0.73×10^{-3}	1.29
0.3, 0.3, 0.15, 0.125; −18, 15	L-18 [spread along x; unscaled]	12.8	0.30×10^{-3}	0.71
0.3, 0.3, 0.6, 0.5; −36, 30	L-19 [peaked along x; scaled 2]	15.1	0.52×10^{-3}	0.42
0.15, 0.15, 0.3, 0.25; −18, 15	L-20 [spread along y]	21.3	0.83×10^{-3}	1.18
0.3, 0.15, 0.3, 0.125; −18, 3.75	L-21 [asymmetric I]	9.5	0.21×10^{-3}	0.52
0.3, 0.075, 0.3, 0.0625; −18, 0.938	L-22 [asymmetric II]	8.8	0.13×10^{-3}	0.49
0.3, 0.075, 0.3, 0.0625; −18, 0.938	L-23 [asymm. II w/15 km lever]	10.2	0.16×10^{-3}	0.57
0.3, 0.0375, 0.3 0.03125; −18, 0.235	L-24 [asymmetric III]	8.9	0.11×10^{-3}	0.50
6. Monopole: nature of source				
Dipole	L-01 (R_L)	11.9	0.37×10^{-3}	0.66
Monopole	L-25	8.4	0.98×10^{-4}	0.47
Positive monopole	L-26	4.9	0.42×10^{-4}	0.33*
7. Water depth: depth to ocean floor, H (m)				
$H = 5000$	L-01 (R_L)	11.9	0.37×10^{-3}	0.66
$H = 4000$	L-27	11.9	0.37×10^{-3}	0.66
$H = 3000$	L-28	11.9	0.36×10^{-3}	0.66
$H = 2000$	L-29	12.4	0.32×10^{-3}	0.69
$H = 5000$	L-04 ($L = 100$ km)	4.9	0.62×10^{-4}	0.27
$H = 4000$	L-30 ($L = 100$ km)	5.3	0.61×10^{-4}	0.30
$H = 3000$	L-31 ($L = 100$ km)	6.3	0.69×10^{-4}	0.35
$H = 2000$	L-32 ($L = 100$ km)	7.5	0.74×10^{-4}	0.42
8. Beach slope: slope to 5000 m, tan β				
1/50	L-33	10.6	0.33×10^{-3}	0.59
1/30	L-34	12.1	0.38×10^{-3}	0.67
1/20	L-01 (R_L)	11.9	0.37×10^{-3}	0.66
1/13	L-35	11.8	0.35×10^{-3}	0.66
9. Composite beaches: tan β_{up}; tan β_{down}				
1/20; 1/20	L-01 (R_L)	11.9	0.37×10^{-3}	0.66
1/50; 1/20	L-36	11.0	0.36×10^{-3}	0.61
1/13; 1/30	L-37	14.3	0.36×10^{-3}	0.80
1/20; 1/500; 1/20	L-38	7.8	0.20×10^{-3}	0.43

*In this case, and since $\eta_- = 0$, I_3 is taken as b/η_+.

As in the case of dislocations, we proceed to vary systematically the various parameters of the model described above and on Fig. 3.

3.2.1 *Distance, L*

Both scalars I_2 and I_3 are found to decrease strongly with increasing distance from the beach, and more so than in the case of dislocations, reflecting the greater dispersion affecting tsunamis generated by landslides. Note that the extreme case analysed here, $L = 100$ km, would lead to $I_2 = 6.2 \times 10^{-5}$, comparable to the upper bound of values found in the worst case dislocation scenario (D-34). However, it is not realistic to expect a landslide on the flat portion of the ocean, seaward of the toe of the beach.

3.2.2 *Pole amplitudes, η_- and η_+*

In this set of models, we change η_- and η_+, but leave unchanged the coefficients α and γ, which are inverse measures of the width of the initial wave (see Fig. 3). This results in a change in the aspect ratios of the initial depression and elevation on the surface of the ocean. We find that the scalar I_3 is practically unchanged, while I_2 increases significantly with source size.

3.2.3 *Dipole lever, l*

The length l of the lever between the two poles of the source is related to the distance travelled by the slide on the ocean bottom. The scalar I_3 is found to increase with l, a result consistent with the 1-D analysis of Tadepalli & Synolakis (1994). A short lever also reduces I_2, while a longer one leaves it relatively unchanged.

3.2.4 *Dipole orientation (azimuth), ϕ*

In these models, we allow the dipole to lie at an angle other than 90° from the coastline. This is a rather improbable geometry, given that any slide is expected to occur along the line of steepest descent, usually perpendicular to the shoreline. We find that a departure from that geometry reduces both scalars, but only moderately.

3.2.5 *Profile of the poles*

Next, we vary the coefficients α and γ, controlling the shape of the initial depression and elevation on the ocean surface. First (Model L-11), we double the width of the source along the y direction (by halving α_- and α_+), but we reduce its amplitude by half (both η_- and η_+), in order to keep unchanged the total amount of fluid displaced at the surface. The result is that I_2 is only slightly changed from the reference model, while I_3 is nearly doubled, to 1.25. As the maximum run-up, b, is practically unchanged (11.3 m versus 11.9 m), this would suggest that the whole run-up distribution, $\zeta(y)$ (both a and b), is controlled by the amount of fluid displaced at the surface rather than the maximum amplitude of that initial displacement. The next model (L-12) is obtained from Model L-11 by doubling the length of the source in the x direction perpendicular to the coast (halving the coefficients γ), and keeping the values of η_- and η_+. Note that we now displace twice as much fluid at the surface, but that this increase occurs entirely along x. We find that the field $\zeta(y)$ is unchanged from the reference model ($b = 11.9$ m, $I_2 = 0.37 \times 10^{-3}$). We verify in Model L-13 that a further reduction in η_- and η_+ decreases the maximum run-up b, but leaves the width of the profile a unchanged.

Thus, our analysis strongly suggests that the amplitude and distribution of run-up are controlled by the surface integral of the cross-section of the source parallel to the beach (the combinations η_-/α_- and η_+/α_+), and largely independent of the parameters γ describing the distribution in the third dimension (x, perpendicular to the beach). With hindsight, this result is implicit in Tadepalli & Synolakis (1994, Fig. 3) and Briggs *et al.* (1993, Fig. 6) (note that $1/\alpha$ is a measure of source length, S in their notation). This interpretation is also supported by the results of models L-14, L-15, L-16 and L-18, which involve narrower, rather than broader, sources. It further suggests that, at the range of distances considered (where $\gamma L \gg 1$), the width a and amplitude b of the run-up distribution are insensitive to the lateral extent of the source along x. The situation differs fundamentally from that of the seismic dislocation, for which the extent of the source is always at least comparable to the distance to shore L, for any earthquake large enough to be tsunamigenic.

Finally, we consider the case of strongly asymmetric dipoles (models L-21 to L-24), in which we leave the depression unchanged from the reference model, but increasingly broaden the elevation in both directions x and y (while reducing its amplitude), to address the case of a slide losing its cohesion and diffusing laterally as it progresses. We find that run-up decreases and becomes more scattered (I_2 decreases).

3.2.6 *Monopole*

We pursue this approach by considering the ultimate asymmetric dipole, i.e. a monopole consisting only of a depression, the balancing elevation being conceptually spread out over the entire ocean ($\eta_+ = 0$, $\alpha_+ = 0$, $\gamma_+ = 0$). This model (L-25) could represent the evolution of the slide into a turbidity current, as documented following a number of underwater landslides (e.g. Heezen & Ewing 1952, 1955). Our results clearly constitute the limiting case of the asymmetric dipoles (models L-21 to L-24). For completeness and despite a lack of physical relevance, we also consider the case of the positive monopole (L-26).

3.2.7 *Water depth, H*

Table 2 shows that basin depth H has practically no influence on the amplitude and distribution of run-up when the source is directly over the sloping beach. This simply expresses the fact that any change in basin depth taking place seaward of the source does not affect the wave propagating towards the shore. Only in the case of the shallowest basin, for which the source is placed near the toe of the slope, does H become relevant.

Of course, if the source is moved out to sea ($L \geq 100$ km), a change in H means a change in the water column below the source, and hence affects the final distribution of run-up (models L-30 to L-32). Note that the amplitude b (and hence I_3) decreases with increasing H; this trend is opposite to that for dislocation sources, because of the different distances L (and hence ratios L/H) involved in both cases. On the other hand, the scalar I_2 is essentially independent of H.

3.2.8 *Slope and shape of beach*

Again, contrary to the case of dislocation sources, we find that the slope of the beach or the presence of a composite beach play only

a very marginal role on the amplitude of run-up and leave I_2 practically unchanged. We attribute this to the fact that, in the case of a dislocation, the source is located farther seaward relative to the toe of the sloping beach, so that reflection at the transition affects the evolution of the wave, as discussed by Synolakis (1987). In contrast, for the landslide source, the relative independence of run-up on the beach slope is consistent with the findings of Liu *et al.* (2003, Fig. 4) for the 1-D evolution of landslide waves generated by moving blocks.

In a final experiment (L-38), we consider the case of our standard slope ($\tan\ \beta = 1/20$), but interrupt it between depths of 100 and 200 m by a 50 km wide continental shelf ($\tan\ \beta = 1/500$). We place the source on the continental slope, at $L = 75$ km from the beach, as in the case of Model L-03, which featured a standard beach slope. We find that the maximum run-up b is practically unchanged, while I_2 increases slightly, and at any rate remains greater than 10^{-4}.

In conclusion, our results from 72 simulations are summarized in Fig. 5, which plots the scalars I_1 (or I_3) and I_2 using logarithmic scales for the two populations of models considered. Focusing first on the scalar I_2, it is clear that the two populations of sources are well separated, with the possible exception of the four landslide data points shown as open circles and for which $I_2 < 10^{-4}$. However, the latter correspond to $L = 100$ km, i.e. to landslide sources occurring in the deep ocean basin. They were included in the database only to glean some understanding of the influence of the parameter L on the distribution of run-up, but are physically unrealistic, since a landslide must occur on a slope. The last experiment (L-38) shows that the presence of a large continental shelf will actually increase the value of I_2. Even the borderline case of the monopole ($I_2 = 0.98 \times 10^{-4}$) is a limiting case abstraction. We conclude that the scalar I_2 constitutes a reliable discriminant of the nature of the source, with any value larger than 10^{-4} being characteristic of a landslide source.

As for the scalars I_1 (or I_3), Fig. 5 shows that they remain of order 1 or smaller. For dislocations, the largest value of I_1, obtained in our worst case scenario, is 1.35. In this respect, we verify the intuitive argument of Plafker (1997) regarding scaling of maximum run-up to fault slip, and confirm that I_1 could also be used as a discriminant of the nature of the source. However, its computation requires the knowledge of the slip Δu, which is always a difficult measurement and may not be available in real time.

4 APPLICATION TO SURVEY DATA SETS

We regroup into a database the run-up profiles surveyed and published by the International Tsunami Survey Teams following eight major tsunamis of the past 12 yr; we also include field data of the great 1946 Aleutian tsunami, surveyed in 2001 at Unimak Island by Okal *et al.* (2003b).

Table 3 lists all relevant information, and in particular the sources of the compiled data sets. Whenever available, the exact coordinates of the locations surveyed were entered in the database, the coastline digitized from a map, and its azimuth (the direction 'y') optimized by regression. We eliminated from this study surveys taken on coastlines which were either too irregular or too fragmented to be adequately approximated by a straight line. This resulted in the exclusion of such cases as the 1994 Mindoro, 1994 Kuriles, 1996 Biak or 1999 Vanuatu tsunamis. Also, we excluded from our profiles points surveyed on offshore islands (e.g. in the 2002 Wewak, PNG event or at Sanak in the case of the 1946 survey). Finally, we also deleted run-up values involving splashing against steep cliffs.

For each event investigated, we proceed to best-fit a profile of the type in eq. (1) to the data set, and list in Table 3 the resulting values of b, a and I_2. In order to compute an estimate of I_1, the slip Δu is inferred from published values of M_0, using the scaling laws of Geller (1976). Note that this approach may result in underestimating Δu if the earthquake features anomalous properties, such as rupture in weak material. However, in the context of using I_1 as a discriminant, possibly in quasi-real time, we prefer to use estimates of Δu derived from scaling laws. The resulting values of I_1 are listed in Table 3, and individual profiles shown on Fig. 6; note that all frames use a common vertical exaggeration of 10 000, so that aspect ratios are directly comparable. The nine events are also shown as triangles (keyed to their Julian dates) in the $\{I_1, I_2\}$ plane on Fig. 5.

The most important result from this investigation is that two earthquakes stand out as clearly anomalous—the 1946 Aleutian and the

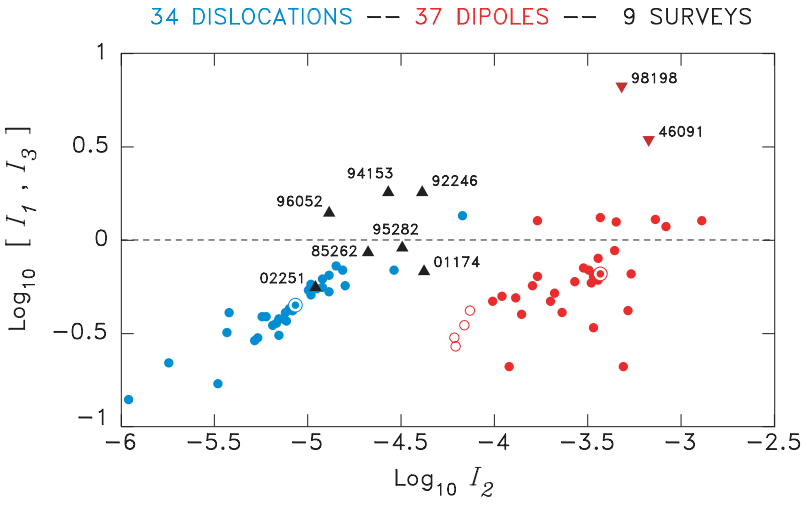

Figure 5. Scalar values I_1 (or I_3) and I_2 obtained for the simulations performed in the present study. The 34 blue dots represent dislocation models; the 37 red ones landslides. The bull's eye symbols identify the reference models (D-01 and L-01). In the case of landslides, the open symbols show the geologically improbable models L-04, L-30, L-31 and L-32, for which $L = 100$ km, i.e. the landslide would have to take place in the flat ocean basin. The triangles (with Julian dates, see Table 3) refer to the survey data sets discussed in Section 4; for all of them the value I_1 is calculated from estimates of M_0 using scaling laws. I_1 is clearly much too large for the 1998 PNG and 1946 Aleutian events, whose values of I_2 are also characteristic of landslides.

Table 3. Field survey data set.

Event	Date (Day Mo (J) Yr)	Epicentre (°N, °E)	Seismic moment, M_0 (10^{27} dyn cm) [Ref.]	Δu (m)	No of survey points [Ref.]	Best-fit parameters			
						b (m)	a (km)	I_1	I_2
Unimak, Aleutians	01 Apr. (091) 1946	53.31, −162.88	80 [a]	9.0	21 [b]	31.0	46	3.4	6.7×10^{-4}
Mexico	19 Sept. (262) 1985	18.19, −102.53	11 [c]	4.3	11 [d]	3.7	176	0.86	2.1×10^{-5}
Nicaragua	02 Sept. (246) 1992	11.74, −87.34	3.4 [e]	2.9	71 [f]	5.4	130	1.8	4.1×10^{-5}
Java	02 June (153) 1994	−10.48, 112.84	5.3 [g]	3.4	54 [h]	6.0	219	1.8	2.7×10^{-5}
Mexico	09 Oct. (282) 1995	19.06, −104.21	11.5 [i]	4.3	34 [j]	4.0	121	0.93	3.2×10^{-5}
Chimbote, Peru	21 Feb. (052) 1996	−9.59, −79.59	2.2 [k]	2.5	42 [l]	3.1	241	1.4	1.3×10^{-5}
Aitape, PNG	17 July (198) 1998	−2.96, 141.93	0.37 [m]	1.4	83 [n]	9.0	19	6.4	4.7×10^{-4}
Camana, Peru	23 June (174) 2001	−16.27, −73.64	47 [o]	6.9	26 [p]	4.7	111	0.68	4.2×10^{-5}
Wewak, PNG	08 Sept. (251) 2002	−3.30, 142.95	3.0 [q]	2.7	36 [q]	1.5	131	0.56	1.2×10^{-5}

References: a, López & Okal (2002); b, Okal *et al.* (2003b); c, Dziewonski *et al.* (1986); d, Abe *et al.* (1986); e, Dziewonski *et al.* (1993); f, Abe *et al.* (1993); g, Dziewonski *et al.* (1995); h, Tsuji *et al.* (1995); i, Dziewonski *et al.* (1997a); j, Borrero *et al.* (1997); k, Dziewonski *et al.* (1997b); l, Bourgeois *et al.* (1999); m, Dziewonski *et al.* (1999); n, Synolakis *et al.* (2002a); o, Ekström *et al.* (2003); p, Okal *et al.* (2002); q, Borrero *et al.* (2003).

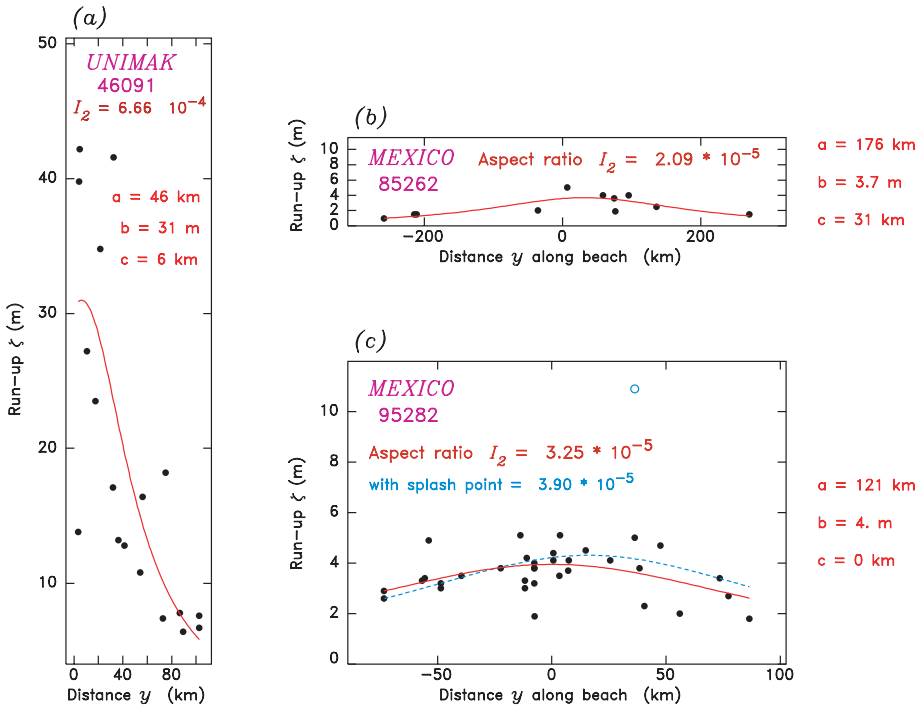

Figure 6. Run-up profiles obtained during surveys of recent tsunamis by the International Tsunami Survey Teams (b–i), and for the 1946 Aleutian event by Okal *et al.* (2003b) on Unimak Island (a) (see Table 3 for relevant details and references). The various frames are identified by Julian dates and arranged sequentially in time. Full dots are the individual points surveyed and open circles show data points involving documented splashes on coastal cliffs, and excluded from the regressions. All nine frames use the same vertical exaggeration of (10^4), allowing direct comparison of the aspect ratios of the various data sets. The red curves are the best-fitting functions of the type of eq. (1), with relevant parameters a, b and c and scalar I_2 listed explicitly on each frame. In (c) and (g), the dashed lines are regressions incorporating the splashes. Note the clearly singular behaviour of the 1998 PNG data set (h), confirming generation by a landslide. In the case of Unimak (a), the absence of data for negative y makes the interpretation more tentative, but the rapid decay of ζ with positive y strongly suggests a similar mechanism.

1998 Aitape, PNG, events, which feature values of both scalars I_1 and I_2 significantly in excess of the range obtained for dislocations in Section 3. They are shown as inverted triangles in Fig. 5. In the case of the Aitape event, our investigation merely quantifies the extreme concentration of the devastation on a short stretch of coastline, as reported for example by Synolakis *et al.* (2002a). The distribution of run-up is somewhat more difficult to interpret for the 1946 earthquake, because of the lack of data to the west of Unimak Island (Okal *et al.* 2003b). However, the very rapid eastward drop of run-up with distance documented in Fig. 6(a) clearly requires a value of I_2 typical of a landslide rather than of a dislocation. By analogy with the case of Aitape, where the occurrence of a landslide is confirmed by independent evidence (Davies *et al.* 2003; Okal 2003a; Sweet & Silver 2003), the analysis of I_2 confirms that the 1946 near-field tsunami on Unimak Island was due to an underwater landslide.

The two landslide events also feature large values of I_1, when this scalar is computed based on seismic slip expected from available estimates of M_0 for the parent earthquakes. For the remaining seven earthquakes, I_1 is at most 1.8, reaching this maximum value for the 1992 Nicaragua and 1994 Java earthquakes, and a slightly lower

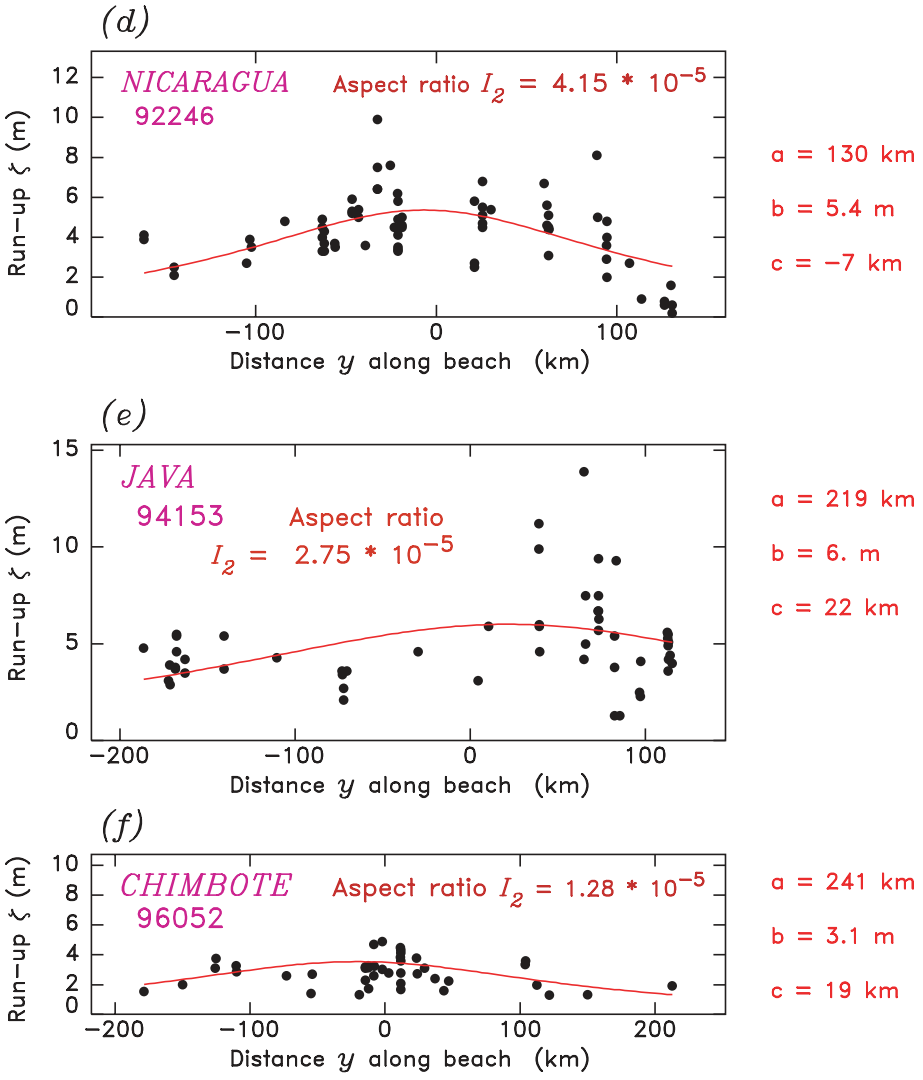

Figure 6. (*Continued.*)

value (1.4) for the 1996 shock at Chimbote, Peru. All three events have been documented as 'tsunami earthquakes' (Newman & Okal 1998; Polet & Kanamori 2000), and the high values of I_1 may be an artefact of underestimating Δu.

Finally, Figs 6(h) and (i) provide a spectacular illustration of the difference between the two PNG tsunamis in 1998 at Aitape and in 2002 at Wewak. As described in detail by Borrero *et al.* (2003), these two earthquakes featured strikingly differing damage, even though their epicentres were only 120 km apart: the 1998 event did practically no structural damage, but its tsunami was devastating, while the stronger 2002 event resulted in widespread destruction, but only a benign tsunami. The interpretation—that an underwater landslide was triggered in 1998 but not in 2002—is clearly supported by the respective values of I_1 (11 times greater in 1998) and I_2 (39 times greater in 1998).

5 CONCLUSION

The simulation of the run-up of a near-field tsunami along a beach for more than 70 scenarios of both dislocation and landslide sources identifies the aspect ratio I_2 as a robust potential discriminant between the two families of sources. It represents the ratio of the maximum run-up b to the characteristic width a of its distribution along the beach, and we infer that it is inherently bounded, in the case of seismic dislocations, by the maximum strain release at the source. Even in a worst case scenario, we find that I_2 remains less than 10^{-4}. By contrast, landslide sources, which concentrate large vertical motions over relatively limited lateral dimensions, lead to higher values of I_2 for all physically realistic combinations of source parameters. Thus, in very simple terms, the threshold $I_2 = 10^{-4}$ could serve as a source discriminant in the near field.

We find that the scalars I_1 and I_3 which scale the maximum run-up b to the initial motions of the source (either the seismic slip Δu for the dislocation or the amplitude of the original depression for the landslide), are also relatively robust, never exceeding a value of 1.5 in all the cases considered. Thus our simulations validate the 'rule of thumb' that a seismic dislocation does not produce run-up much in excess of its own amplitude of slip on a nearby beach with a smooth topography, and the concept of using I_1 as a further discriminant of the nature of the source.

In the aftermath of a local tsunami, and notwithstanding the difficulty of obtaining a preliminary model of the seismic source, widely available real-time estimates of the seismic moment (e.g.

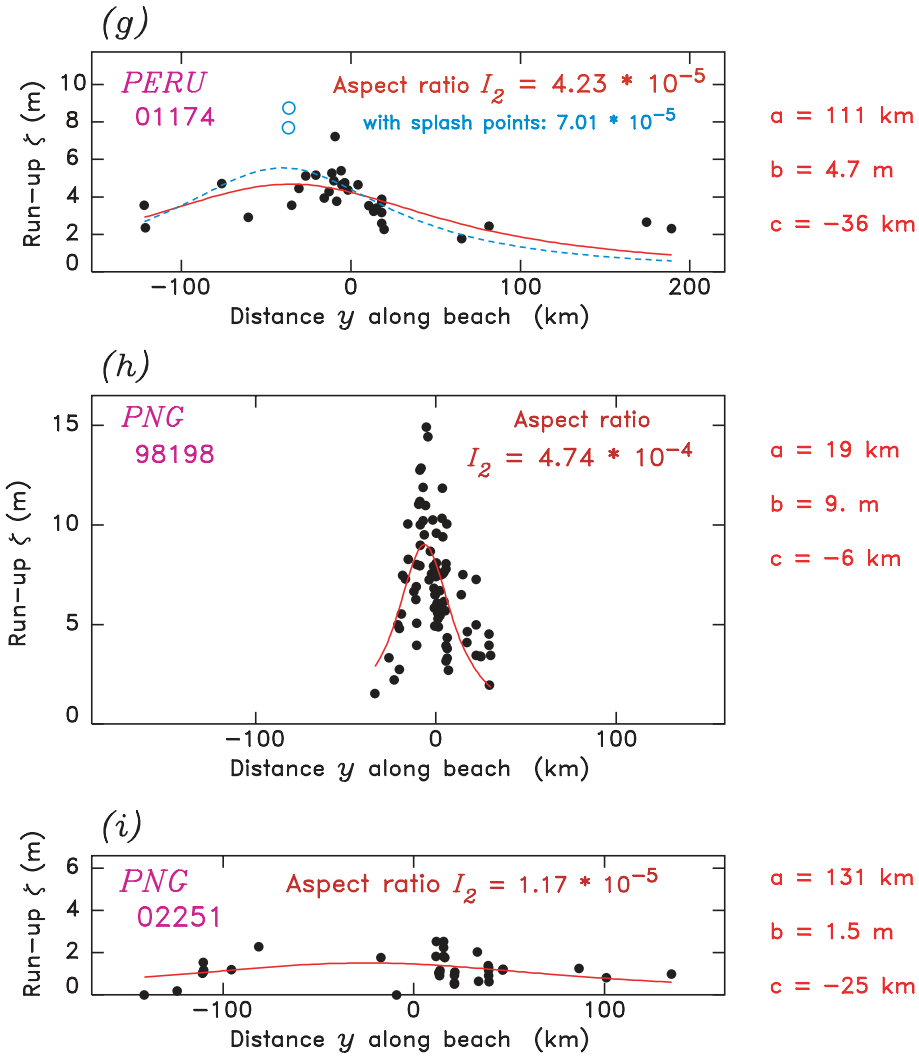

Figure 6. (*Continued.*)

Okal & Talandier 1989) can give an order of magnitude of the slip Δu expected under scaling laws, and thus a value of I_1 can be inferred from a field survey. Our analyses show that excessive values of I_1, corresponding to run-up amplitudes reaching five times or more the values of the seismic slip Δu, are simply incompatible with tsunami generation by a dislocation. Indeed, such a mismatch was the crucial evidence behind the early suggestion that a submarine landslide had to be involved in the source of the 1998 PNG earthquake (Synolakis *et al.* 1998).

ACKNOWLEDGMENTS

We thank our field companion, George Plafker, for discussing his 'rule of thumb' concept during nights of endless twilight on the windswept Aleutians. This research was supported by the National Science Foundation, most recently under grants CMS-0301054 to EAO and CMS-0301081 to CES. We are grateful to Dr Cliff Astill for his visionary support of field surveys and analysis that made most tsunami work in the past decade possible. We thank Fred Raichlen and an anonymous scientist for their reviews of the original manuscript. Raiden Hasegawa of Evanston Township High School helped with compilation and initial processing of the field survey database, acquired through the hard field work of our many colleagues from the International Survey teams; they are too numerous to list individually.

REFERENCES

Abe, K. et al, 1993. Field survey of the Nicaragua earthquake and tsunami of September 2, 1992, *Bull. Earthquake Res. Inst. Tokyo Univ.,* **68,** 23–70.

Abe, K., Hakuno, M., Takeuchi, M. & Katada, T., 1986. Survey report on the tsunami of the Michoacan, Mexico earthquake of September 19, 1985, *Bull. Earthquake Res. Inst. Tokyo Univ.,* **61,** 475–481.

Borrero, J.C., Ortiz, M., Titov, V. & Synolakis, C., 1997. Field survey of Mexican tsunami produces new data, unusual photos, *EOS, Trans. Am. geophys. Un.,* **78,** 85, 87–88.

Borrero, J.C., Dolan, J.F. & Synolakis, C.E., 2001. Tsunamis within the Eastern Santa Barbara Channel, *Geophys. Res. Lett.,* **28,** 643–646.

Borrero, J.C., Bu, J., Saiang, C., Uslu, B., Freckman, J., Gomer, B., Okal, E.A. & Synolakis, C.E., 2003. Field survey and preliminary modeling of the Wewak, Papua New Guinea earthquake and tsunami of September 9, 2002, *Seism. Res. Lett.,* **74,** 393–405.

Bourgeois, J. et al, 1999. Geologic setting, field survey and modeling of the Chimbote, Northern Peru, tsunami of 21 February 1996, *Pure appl. Geophys.,* **154,** 513–540.

Briggs, M.J., Synolakis, C.E. & Hughes, S.A., 1993. Laboratory measurements of tsunami run-up, in, *Proc. IUGG/IOC International Tsunami Symposium, August 23–27, 1993,* pp. 585–598, eds Tsuchiya, Y. & Shuto, N., Japan Society for Civil Engineering, Wakayama.

Davies, H.L., Davies, J.M., Perembo, R.C.B. & Lus, W.Y., 2003. The Aitape 1998 tsunami: reconstructing the event from interviews and field mapping, *Pure appl. Geophys.,* **160,** 1895–1922.

Dziewonski, A.M., Friedman, A., Giardini, D. & Woodhouse, J.H., 1983. Global seismicity of 1982: centroid moment tensor solutions for 308 earthquakes, *Phys. Earth planet. Inter.,* **33,** 76–90.

Dziewonski, A.M., Franzen, J.E. & Woodhouse, J.H., 1986. Centroid moment-tensor solutions for July–September 1985, *Phys. Earth planet. Inter.,* **42,** 205–214.

Dziewonski, A.M., Ekström, G. & Salganik, M.P., 1993. Centroid-moment tensor solutions for July–September 1992, *Phys. Earth planet. Inter.,* **79,** 287–297.

Dziewonski, A.M., Ekström, G. & Salganik, M.P., 1995. Centroid-moment tensor solutions for April–June 1994, *Phys. Earth planet. Inter.,* **88,** 69–78.

Dziewonski, A.M., Ekström, G. & Salganik, M.P., 1997a. Centroid-moment tensor solutions for October–December 1995, *Phys. Earth planet. Inter.,* **101,** 1–12.

Dziewonski, A.M., Ekström, G. & Salganik, M.P., 1997b. Centroid-moment tensor solutions for January–March 1996, *Phys. Earth planet. Inter.,* **102,** 1–9.

Dziewonski, A.M., Ekström, G. & Maternovskaya, N., 1999. Centroid-moment tensor solutions for July-September 1998, *Phys. Earth planet. Inter.,* **114,** 99–107.

Ekström, G., Dziewoński, A.M., Maternovskaya, N.N. & Nettles, M., 2003. Global seismicity of 2001: centroid-moment tensor solutions for 961 earthquakes, *Phys. Earth planet. Inter.,* **136,** 165–185.

Ewing, M., Tolstoy, I. & Press, F., 1950. Proposed use of the T phase in tsunami warning systems, *Bull. seism. Soc. Am.,* **40,** 53–58.

Green, G., 1838. On the motion of waves in a variable canal of small depth and width, *Proc. Camb. Phil. Soc.,* **6,** 457–462.

Geller, R.J., 1976. Scaling relations for earthquake source parameters and magnitudes, *Bull. seism. Soc. Am.,* **66,** 1501–1523.

Gutenberg, B., 1939. Tsunamis and earthquakes, *Bull. seism. Soc. Am.,* **29,** 517–526.

Heezen, B.C. & Ewing, M., 1952. Turbidity currents and submarine slumps, and the 1929 Grand Banks earthquake, *Am. J. Sci.,* **250,** 849–873.

Heezen, B.C. & Ewing, M., 1955. Orléansville earthquake and turbidity currents, *Bull. Am. Assoc. Petrol. Geol.,* **39,** 2505–2514.

Heinrich, P., Piatanesi, A., Okal, E.A. & Hébert, H., 2000. Near-field modeling of the July 17, 1998 tsunami in Papua New Guinea, *Geophys. Res. Lett.,* **27,** 3037–3040.

Kanamori, H. & Kikuchi, M., 1993. The 1992 Nicaragua earthquake; a slow tsunami earthquake associated with subducted sediments, *Nature,* **361**, 714–716.

Kánoğlu, U. & Synolakis, C.E., 1998. Long wave runup on piecewise linear topographies, *J. Fluid Mech.,* **374,** 1–28.

Kulikov, E.A., Rabinovich, A.B., Thomson, R.E. & Bornhold, B.D., 1996. The landslide tsunami of November 3, 1994, Skagway harbor, Alaska, *J. geophys. Res.,* **101,** 6609–6615.

Lee, H.J., Kayen, R.E., Gardner, J.V. & Locat, J., 2003. Characteristics of several tsunamigenic submarine landslides, in *Submarine Mass Movements and Their Consequences,* pp. 357–366, eds Locat, J. & Mienert, J., Dordrecht, Kluwer.

Liu, P.L.-F., Lynett, P. & Synolakis, C.E., 2003. Analytical solutions for forced long waves on a sloping beach, *J. Fluid Mech.,* **478,** 101–109.

López, A.M. & Okal, E.A., 2002. Aftershock relocation, rupture area, mantle magnitude and energy estimates of the 1946 Aleutian tsunami earthquake and neighboring events, *EOS, Trans. Am. geophys. Un.,* **83**(47), F1045 (abstract).

Mansinha, L. & Smylie, D.E., 1971. The displacement fields of inclined faults, *Bull. seism. Soc. Am.,* **61,** 1433–1440.

Milne, J., 1898. *Earthquakes and Other Earth Movements,* Paul, Trench, Trubner & Co., London.

Montessus de Ballore, F., 1907. *La Science Séismologique,* A. Colin, Paris.

Newman, A.V. & Okal, E.A., 1998. Teleseismic estimates of radiated seismic energy: The E/M_0 discriminant for tsunami earthquakes, *J. geophys. Res.,* **103**, 26 885–26 898.

Okal, E.A., 1988. Seismic parameters controlling far-field tsunami amplitudes: a review, *Natural Hazards,* **1**, 67–96.

Okal, E.A., 2003a. *T* waves from the 1998 Papua New Guinea earthquake and its aftershocks: timing the tsunamigenic slump, *Pure appl. Geophys.,* **160**, 1843–1863.

Okal, E.A., 2003b. Normal modes energetics for far-field tsunamis generated by dislocations and landslides, *Pure appl. Geophys.,* **160**, 2189–2221.

Okal, E.A. & Synolakis, C.E., 2003. Theoretical comparison of tsunamis from dislocations and landslides, *Pure appl. Geophys.,* **160**, 2177–2188.

Okal, E.A. & Talandier, J., 1989. M_m: a variable period mantle magnitude, *J. geophys. Res.,* **94**, 4169–4193.

Okal, E.A. et al, 2002. A field survey of the Camana, Peru tsunami of June 23, 2001, *Seism. Res. Lett.,* **73**, 904–917.

Okal, E.A., Synolakis, C.E., Borrero, J.C. & Members of the ITSTs, 2003a. 1992–2002: perspective on a decade of tsunami field surveys, *EOS, Trans. Am. geophys. Un.,* **84**(46), F805 (abstract).

Okal, E.A., Plafker, G., Synolakis, C.E. & Borrero, J.C., 2003b. Near-field survey of the 1946 Aleutian tsunami on Unimak and Sanak Islands, *Bull. seism. Soc. Am.,* **93**, 1226–1234.

Plafker, G., 1965. Tectonic deformation associated with the 1964 Alaskan earthquake, *Science,* **148**, 1675–1687.

Plafker, G., 1997. Catastrophic tsunami generated by submarine slides and backarc thrusting during the 1992 earthquake on eastern Flores I., Indonesia, *Geol. Soc. Am. Cordill. Sect.,* **29**, 57 (abstract with programme).

Plafker, G. & Savage, J.C., 1970. Mechanism of the Chilean earthquakes of May 21 and 22, 1960, *Geol. Soc. Am. Bull.,* **81**, 1001–1030.

Pod"yapol'skii, G.S., 1970. Generation of the tsunami wave by the earthquake, in *Tsunamis in the Pacific Ocean,* pp. 19–32, ed. Adams, W.M., East–West Center Press, Honolulu.

Polet, J. & Kanamori, H., 2000. Shallow subduction zone earthquakes and their tsunamigenic potential, *Geophys. J. Int.,* **142**, 684–702.

Satake, K. & Kanamori, H., 1991. Abnormal tsunamis caused by the June 13, 1984, Tori-shima, Japan, earthquake, *J. geophys. Res.,* **96**, 19 933–19 939.

Satake, K. & Tanioka, Y., 2003. The July 1998 Papua New Guinea earthquake: mechanism and quantification of unusual tsunami generation, *Pure appl. Geophys.,* **160**, 2087–2118.

Schwarz, H.-U., 1982. *Subaqueous slope failures—Experiments and Modern Occurrences,* E. Schweizerbart'sche Verlagsbuchhandlung, Stuttgart.

Sweet, S. & Silver, E.A., 2003. Tectonics and slumping in the source region of the 1998 Papua New Guinea tsunami from seismic reflection images, *Pure appl. Geophys.,* **160**, 1945–1968.

Synolakis, C.E., 1987. The runup of solitary waves, *J. Fluid Mech.,* **185**, 523–545.

Synolakis, C.E., 1991. Green's law and the evolution of solitary waves, *Phys. Fluids, Ser. A,* **3**, 490–492.

Synolakis, C.E. & Skjelbreia, E.J., 1993. The four zones in the evolution of solitary waves on plane beaches, *J. Waterw. Ports Coastal Eng.,* **118**, 252–266.

Synolakis, C.E., Okal, E.A., Borrero, J.C., Benson, B., Nott, J. & de Lange, W.P., 1998. Preliminary report of the ITST—the Western and Island Coasts, *EOS, Trans. Am. geophys. Un.,* **79** (45), F563 (abstract).

Synolakis, C.E., Bardet, J.-P., Borrero, J.C., Davies, H.L., Okal, E.A., Silver, E.A., Sweet, S. & Tappin, D.R., 2002a. The slump origin of the 1998 Papua New Guinea tsunami, *Proc. R. Soc. Lond.,* A, **458**, 763–789.

Synolakis, C.E., Yalçiner, A.C., Borrero, J.C. & Plafker, G., 2002b. Modeling of the November 3, 1994 Skagway, Alaska tsunami, in *Solutions to Coastal Disasters,* pp. 915–927, eds Wallendorf, L. & Ewing, L., American Society for Civil Engineering, Reston.

Tadepalli, S. & Synolakis, C.E., 1994. The runup of *N* waves, *Proc. R. Soc. Lond.,* A, **445**, 99–112.

Tinti, S. & Bortolucci, E., 2000. Energy of water waves induced by submarine landslides, *Pure appl. Geophys.,* **157**, 281–318.

Titov, V.V. & Synolakis, C.E., 1998. Numerical modeling of tidal wave runup, *J. Waterw. Ports Coast. Ocean Eng.,* **124**, 157–171.

Tsuji, Y. et al, 1995. Field survey of the East Java earthquake and tsunami of June 3, 1994, *Pure appl. Geophys.,* **144**, 839–874.

Ward, S.N., 1980. Relationship of tsunami generation and an earthquake source, *J. Phys. Earth,* **28**, 441–474.

Ward, S.N., 2002. Tsunamis, in, *Encyclopedia of Physical Science and Technology,* 3rd edn, pp. 175–191, ed. Meyers, R.A., Academic Press, New York.

Wu, F.T. & Kanamori, H., 1973. Source mechanism of the February 4, 1965 Rat Island earthquake, *J. geophys. Res.,* **78**, 6082–6092.

Yamashita, T. & Sato, R., 1974. Generation of tsunami by a fault model, *J. Phys. Earth,* **22**, 415–440.